Enhanced Synchronization Stability of Grid-Forming Inverters With Passivity-Based Virtual Oscillator Control

Le Kong, *Student Member, IEEE*, Yaosuo Xue, *Senior Member, IEEE*, Liang Qiao, *Student Member, IEEE*, and Fei Wang, *Fellow, IEEE*

***Abstract*—In this article, a passivity-based virtual oscillator control strategy with enhanced synchronization stability for grid-forming inverters (GFMs) is proposed. By adopting the port-controlled Hamiltonian system theory for orbital stabilization problems, an energy pumping-and-damping block is proposed to render GFMs globally asymptotically stable with respect to the prespecified solutions of the power-flow equations from any initial condition. This allows for stable integrations of GFMs to any other globally asymptotically stable systems without their explicit knowledge, e.g., helping maintain synchronism with the bulk power system in a wide range of short-circuit-ratio conditions or under large disturbances and keeping synchronism among multiple GFMs in power systems. Both simulations and experiments are presented to demonstrate the proposed control approach.**

***Index Terms*—Grid forming inverter, port-Hamiltonian system, synchronization stability, virtual oscillator control.**

I. Introduction

With increasing inception of power electronics interfaced resources and loads in utility power grids, including wind turbine generators, photovoltaic generators, battery energy storage, and electric vehicle charging station, the grid-forming inverters (GFMs) have been adopted to address the issues of high penetration of power electronics and to improve grid stability and resiliency [1], [2]. The control approaches used in these existing GFMs can be roughly classified as two types based on their closed-loop behaviors [3], [4]: 1) mimicking the physical behaviors of the synchronous generators (SGs) and 2) mimicking the physical behaviors of the coupled harmonic oscillators (CHO). The first type of control strategies adopts the well-established theory/approaches for SGs and operates the inverters following the same dynamic equations. On the one hand, this SG-emulation strategy is compatible with the legacy power system. But on the other hand, the characteristics of the power electronics device are different from the SG. The former (i.e., the power electronics device) is with fast actuation, almost no inertia, and limited current capability while the latter (i.e., the SG) is with slow actuation, large enough inertia, and large current capability. The SG-based control cannot intrinsically take the power electronics characteristics into consideration.

The second type of control strategies for GFMs is to mimic the spontaneous synchronization behaviors of CHOs in complex networks. For example, the power-frequency (*p-f*) droop control, as one of the most popular controls for GFMs, can be precisely modeled by the nonuniform multirate Kuramoto-type first-order coupled phase oscillators [5]–[7]. However, the *p-f* droop control only considers phase dynamics of the oscillators, with the oscillation amplitude assumed at a fixed value. To emulate both the phase and magnitude dynamics of CHO, certain control methods, referred as the basic virtual oscillator control (basic VOC), have been developed [8], [9], including the dead-zone VOC and the Van der Pol VOC, but the power sharing of each GFM relies on the load and power network parameters [10], [11]. Therefore, to have a power dispatchable capability, a method called dispatchable VOC (dVOC) has been developed in [4], which offers seamless control of the active and reactive power of the GFM.

One critical challenge for all these control methods is to maintain *synchronization stability*, i.e., keep synchronism with the power network in large-scale power systems under variable grid conditions and with multiple inverters [2], including the following scenarios.

(SC1) The inverters should be able to maintain synchronism in the grids with different grid short-circuit-ratios (SCRs) under small disturbances.

(SC2) GFMs should maintain system *transient stability* under large disturbances, such as load dispatch, fault, and line impedance variations.

Manuscript received 24 February 2022; revised 9 May 2022; accepted 26 June 2022. Date of publication 30 June 2022; date of current version 6 September 2022. This work was supported in part by the U.S. Department of Energy, Office of Electricity, Advanced Grid Modeling Program under Grant DE-AC05-00OR22725, in part by the Engineering Research Program of the National Science Foundation and the DOE through National Science Foundation under Grant EEC1041877, and in part by the CURENT. Recommended for publication by Associate Editor S. Golestan. *(Corresponding author: Le Kong.)*

Le Kong and Liang Qiao are with the Department of Electrical Engineering and Computer Science, The University of Tennessee, Knoxville, TN 37996 USA (e-mail: lkong4@vols.utk.edu; lqiao1@vols.utk.edu).

Yaosuo Xue is with the Electrification and Energy Infrastructures Division, Oak Ridge National Laboratory, Oak Ridge, TN 37830 USA (e-mail: yx@ieee.org).

Fei Wang is with the Department of Electrical Engineering and Computer Science, The University of Tennessee, Knoxville, TN 37996 USA, and also with Oak Ridge National Laboratory, Oak Ridge, TN 37830 USA (e-mail: fred.wang@utk.edu).

Color versions of one or more figures in this article are available at https://doi.org/10.1109/TPEL.2022.3187402.

Digital Object Identifier 10.1109/TPEL.2022.3187402

(SC3) For systems with many small-to-medium and distributed GFMs, it is important to have a decentralized control method so that the GFMs are capable of maintaining system *synchronous stability* in a local way [12].

Note that the *transient stability* [13], [14] is the ability of a power system to remain in synchronism when subjected to severe disturbances, and it is a special case of the more general *rotor angle stability,* which is defined as the system's ability to maintain synchronism after either a small disturbance or a large disturbance. Both the *rotor angle stability* and its special case *transient stability* are the stability issues defined in conventional power systems dominated by SGs. S*ynchronization stability* is an emerging concept to depict the stability issues induced when power electronics inverters are synchronized to a grid. The synchronization stability includes small-signal sideband oscillations of the fundamental frequency, small-signal synchronous oscillations, and large-signal transient stability, all of which are related to power inverter synchronization control. The synchronization stability for power inverters corresponds to the *rotor angle stability* of SGs in today's power systems [2], [15].

Existing control approaches all have some limits in solving these synchronization problems in the abovementioned three scenarios (SC1–SC3) in large-scale power systems with variable grid conditions and multiple inverters. For example, using the most popular *p-f* droop control approach with existing theoretical findings about the Kuramoto oscillators, the system stability conditions can be obtained; however, the entire system information is required for the droop coefficients design, which is not feasible for a variable large-scale power electronics-dominant system. Moreover, despite the existing *p-f* droop control can keep system synchronization stability in a low-SCR grid [16], it tends to have small-signal synchronization instability issues in stiff grids when a low-pass filter (LPF) is embedded in the power loop [17]. The basic VOC methods could be applied to GFMs to globally stabilize the system through only local design based on the $\mathcal{L}_2$ input–output stability criterion without explicit system information, but they cannot dispatch power to the system. The power dispatchable capability can be obtained by the dVOC approach, but to ensure system global asymptotic stability, it requires the knowledge of the underlying dynamics of the entire system, such as the system Laplacian matrix, the set points at all the nodes, and the transmission line parameters [4], [18]–[20]. Recent work on a generic SG-emulation control framework is developed in [21]. It adopts the passivity-based port-Hamiltonian (pH) system theory to render the power electronic system passive with only assuming the load is passive, either in grid-connected mode or islanded mode. This approach is promising in solving these synchronization problems since the lossless interconnection of passive inverters forms a passive system [22]–[24]. However, it has not completely bridged the gap between passivity and stability yet [21]. Additionally, the approach in [21] uses a three-channel structure, where the first channel is for torque, the second channel is the dual to torque, and the third channel is only for lossless interconnection in pH system structure without any physical meanings.

Therefore, in this article, adopting the pH system theory, a passivity-based VOC method to ensure the global asymptotic stability with a clearly defined region of attraction [25] is proposed considering the following aspects.

1) The Hamiltonian function in the passivity-based pH system theory can be naturally chosen as a candidate of the Lyapunov function so that the system stability region can be defined [26], [27].
2) The pH-based passivity concept used in this paper is a nonlinear time-domain solution, so unlike the existing linear passivity-based control approaches, which either only focus on the small-signal harmonic stability issues [28]–[32] or the small-signal synchronization stability [33], it can guarantee system stability under large disturbances in the region of attraction.
3) If each subsystem is globally asymptotically stable (GAS) and if the interconnections are stability preserving, then the overall interconnected system will be GAS [34]. Therefore, it would be feasible for stable integration of multiple inverters since as long as all the inverters are designed to be GAS, the stability of the entire system in the domain of attraction can be guaranteed when they are interconnected.

Hence, the new contribution of this article lies in that the proposed control strategy can guarantee system *synchronization stability* from any initial condition without the need for explicit system information, which is achieved by incorporating the characteristics of spontaneous synchronization of CHOs in complex networks and the passivity-based energy pumping-and-damping motion.

The rest of this article is organized as follows. Section II describes the GFMs with the general VOC method and its corresponding pH model. In Section III, a passivity-based control approach is proposed based on port-controlled Hamiltonian theory. Section IV presents the theoretical stability analysis results of the proposed approach and the comparative case studies with existing approaches. Section V provides the design recommendation of control parameters considering the dynamic response of GFMs, in addition to the stability-related criteria. Simulation and experimental results are presented in Section VI. Finally, Section VII concludes this article.

II. Modeling of GFMs With General VOC in Port-Hamiltonian Framework

A. GFMs With General VOC Approach

There is a close connection between CHOs and the control of power inverters because of the synchronization of inverters pertaining to the synchronization of CHOs. Therefore, in this article, we rely on controlling the GFMs to behave like the Stuart–Landau (SL) oscillators owing to two considerations [35]–[38]. First, the harmonic oscillation pattern of the SL

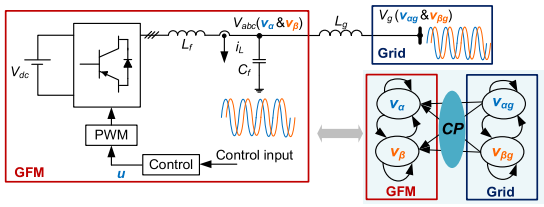

Fig. 1. Grid-connected GFM with a general VOC approach.

oscillator has a clear mapping to the voltage pattern in power systems. That is, the oscillators represented in Cartesian coordinates can describe the two voltage vectors (v_α and v_β) in power system, which are transformed from three-phase voltage through Clark transformation. Second, it is easy to develop coupling terms in an analytical form for multiple coupled SL oscillators using the ac power flow analysis results of the power grids.

Accordingly, the entire power grid can be modeled as (1) in polar coordinates [37], [39], where, ω_k is the natural frequency of oscillator k, γ_{ki}/μ_{ki} is the dissipative/reactive coupling strength between interacting oscillators, v_{refk} is the reference value of the oscillation amplitude, and $v_k(=\rho_k\, e^{i\theta_k})$ is a complex variable with ρ_k being the amplitude of oscillator k and θ_k being its phase angle. The model in (1) can also be reformatted in Cartesian coordinates as given in (2), where $v_k = v_{\alpha k} + jv_{\beta k}$. Furthermore, since this article is aimed to design a local control approach for GFMs to ensure the stability of the entire system without the knowledge of the rest of the system, the problem can then be simplified as two CHOs, as shown in Fig. 1 with a single-directional coupling that is from grid to GFM without loss of generality. This is because, in the design of grid-connected GFMs, the grid can be assumed as an ideal three-phase voltage source, which can be modeled as a coupled harmonic oscillator $v_{\alpha g}$ and $v_{\beta g}$ through Clarke transformation. And the GFM can be controlled as coupled harmonic oscillators v_α and v_β. Also, to have the power dispatching capability, the power flowing through interconnected lines between the grid and the inverter should be controlled, so the power flow can be considered as the coupling effect from the grid oscillator to the inverter oscillator.

In this oscillator-based model, there are two types of couplings in between: one is the internal coupling between v_α and v_β through the oscillation frequency, and the other is the external coupling between the inverter oscillator and grid oscillator, which is physically coupled by the power flow among the connecting lines. As shown in (3), which is simplified from (2) by considering two groups of coupled harmonic oscillators, ω_o is the system fundamental frequency, and the terms in the square brackets are the measure of coupling strength $CP_{\alpha,ref}$ and $CP_{\beta,ref}$ between the GFM and the grid. The coupling strength term can be further modeled by the power flow analysis results, as given in (4), for a well-synchronized system, where γ and μ is defined by the power system parameters, as given in (5), with L_g being the impedance and R being the equivalent resistance of the connecting line between GFM and grid.

More details on the derivation process can be seen in Appendix A

$$\dot{v}_k = \left(v_{refk}^2 + j\omega_k - |v_k|^2\right)\, v_k + \sum_{i=1}^{N} (\gamma_{ki} + j\mu_{ki})\,(v_i - v_k) \quad (1)$$

$$\begin{cases} \dot{v}_{\alpha k} = \left(v_{refk}^2 - v_k^2\right)\, v_{\alpha k} - \omega_k v_{\beta k} + \sum_{i=1}^{N} \\ [\gamma_{ki}\,(v_{\alpha i} - v_{\alpha k}) - \mu_{ki}\,(v_{\beta i} - v_{\beta k})\,] \\ \dot{v}_{\beta k} = \left(v_{refk}^2 - v_k^2\right)\, v_{\beta k} + \omega_k v_{\alpha k} + \sum_{i=1}^{N} [\gamma_{ki}\,(v_{\beta i} - v_{\beta k}) \\ + \mu_{ki}\,(v_{\alpha i} - v_{\alpha k})] \end{cases} \quad (2)$$

$$\begin{cases} \dot{v}_\alpha = \left(v_{ref}^2 - v^2\right) v_\alpha - \omega_o v_\beta + [\gamma\,(v_{\alpha g} - v_\alpha) - \mu(v_{\beta g} - v_\beta)] \\ \dot{v}_\beta = \left(v_{ref}^2 - v^2\right)\, v_\beta + \omega_o v_\alpha + [\gamma\,(v_{\beta g} - v_\beta) + \mu\,(v_{\alpha g} - v_\alpha)] \end{cases} \quad (3)$$

$$\begin{bmatrix} CP_{\alpha,ref} \\ CP_{\beta,ref} \end{bmatrix} = \begin{bmatrix} \gamma\,(v_{\alpha g} - v_\alpha) - \mu\,(v_{\beta g} - v_\beta) \\ \gamma\,(v_{\beta g} - v_\beta) + \mu\,(v_{\alpha g} - v_\alpha) \end{bmatrix} = \frac{1}{v^2} \begin{bmatrix} -Q_{ref} & P_{ref} \\ -P_{ref} & -Q_{ref} \end{bmatrix} \begin{bmatrix} v_\alpha \\ v_\beta \end{bmatrix}. \quad (4)$$

It can then be inferred that to mimic the behavior of CHOs, the controller of GFMs should follow the control structure as given in (6), where ξ_1 is the Hopf bifurcation parameter that controls the convergence speed of the trajectory onto the attractor, ξ_2 is a tuning gain for the coupling strength of the reactive power loop, and ξ_3 is the tuning gain for the coupling strength of the active power loop. Note that the initial conditions for the first-order differential equations (6) should avoid the origin point to initiate an oscillation

$$\begin{cases} \gamma = \frac{\omega_o L_g}{R^2 + (\omega_o L_g)^2} \\ \mu = \frac{R}{R^2 + (\omega_o L_g)^2} \end{cases} \quad (5)$$

$$\begin{bmatrix} \dot{v}_\alpha \\ \dot{v}_\beta \end{bmatrix} = \begin{bmatrix} O_{C11} & O_{C12} \\ O_{C21} & O_{C22} \end{bmatrix} \begin{bmatrix} v_\alpha \\ v_\beta \end{bmatrix} \quad (6)$$

where

$$O_{C11} = O_{C22} = \xi_1\, \left(v_{ref}^2 - v^2\right) + \xi_2 \left(\frac{Q_{ref}}{v_{ref}^2} - \frac{Q}{v^2}\right) \quad (7)$$

$$O_{C21} = -\, O_{C12} = \omega_o + \xi_3 \left(\frac{P_{ref}}{v_{ref}^2} - \frac{P}{v^2}\right). \quad (8)$$

The control dynamics introduced in (6) is a general form of the CHO-emulation control strategies with (7) describing the amplitude dynamics and (8) describing the frequency dynamics of the oscillator. For example, if the amplitude dynamics of the inner oscillations are ignored, it can be simplified as the conventional active power-frequency (*p-f*) and reactive power-voltage (*Q-v*) droop control loops, as will be shown later in Section V-B; if the external coupling effects from the active power and reactive

power are ignored ($\xi_2 = \xi_3 = 0$), it can be simplified as the basic VOC method; while if the tuning gains of the coupling strength in the reactive and active power loop are the same ($\xi_2 = \xi_3$), it will be equivalent to dVOC approach in [4] and [20], furthermore, if the reference voltage is equal to the real voltage in the outer power coupling term ($v_{ref}^2 = v^2$), it can be further simplified as the dVOC method in [19] and [40].

B. Open-Loop and Closed-Loop Models of GFMs With General VOC in pH Framework

1) Open-Loop pH Model: The open-loop pH model of the GFM in Fig. 1 is derived as (9) [26], where the state vector $x = [\varphi_{L\alpha}\ \varphi_{L\beta}\ q_\alpha\ q_\beta]^T = [L_f i_{L\alpha}\ L_f i_{L\beta}\ C_f v_\alpha\ C_f v_\beta]^T$, which are the inductor flux and capacitor charge, $\mathcal{J}_P = -\mathcal{J}_P^T$ is the interconnection matrix as in (10), $\mathcal{R}_P = \mathcal{R}_P^T \geq 0$ is the damping matrix as in (11), $G(x)$ is control matrix as in (12), the u and y are the input and output pairs of the system, and ξ is the external interaction variables as in (13). Note that u represents an ideal voltage source (control vectors in the closed-loop) because the switching frequency of an inverter is much higher than the fundamental frequency, the switching effect can be ignored. In addition, the open-loop Hamiltonian function $H_o(x)$ is a smooth function of the states representing the total inductor and capacitor energy, as given in (14), and its gradient called variable of coenergy $\nabla H_o(x) = \frac{\partial H_o}{\partial x} = [i_{L\alpha}\ i_{L\beta}\ v_\alpha\ v_\beta]^T$

$$\begin{cases} \dot{x} = (\mathcal{J}_P - \mathcal{R}_P)\ \nabla H_o(x) + G(x)\, u + \xi \\ y = G^T(x) \nabla H_o(x) \end{cases} \tag{9}$$

$$\mathcal{J}_P = \begin{bmatrix} 0 & 0 & -1 & 0 \\ 0 & 0 & 0 & -1 \\ 1 & 0 & 0 & 0 \\ 0 & 1 & 0 & 0 \end{bmatrix} \tag{10}$$

$$\mathcal{R}_P = \begin{bmatrix} R_f & 0 & 0 & 0 \\ 0 & R_f & 0 & 0 \\ 0 & 0 & 0 & 0 \\ 0 & 0 & 0 & 0 \end{bmatrix} \tag{11}$$

$$G(x) = \begin{bmatrix} 1 & 0 \\ 0 & 1 \\ 0 & 0 \\ 0 & 0 \end{bmatrix} \tag{12}$$

$$\xi = \begin{bmatrix} 0 & 0 \\ 0 & 0 \\ -1 & 0 \\ 0 & -1 \end{bmatrix} \begin{bmatrix} i_{g\alpha} \\ i_{g\beta} \end{bmatrix} \tag{13}$$

$$H_o(x) = \frac{1}{2} L_f i_{L\alpha}^2 + \frac{1}{2} L_f i_{L\beta}^2 + \frac{1}{2} C_f v_\alpha^2 + \frac{1}{2} C_f v_\beta^2. \tag{14}$$

2) Desired Closed-Loop pH Model: The desired closed-loop pH model combing the general VOC dynamics in (6) is given in (15), where, $\mathcal{J}_d(x)$ is given in (16) and $\mathcal{R}_d(x)$ is given in (17) with b_{34} and b_{43} given in (18), a_{11} and a_{22} given in (19), a_{33} and a_{44} given in (20), and ξ_4 is the current loop control gain. Also, the desired closed-loop Hamiltonian function $H_d(x)$ is given in (21)

$$\dot{x} = (\mathcal{J}_d(x) - \mathcal{R}_d(x))\ \nabla H_d(x) \tag{15}$$

$$\mathcal{J}_d(x) = \begin{bmatrix} 0 & 0 & 0 & 0 \\ 0 & 0 & 0 & 0 \\ 0 & 0 & 0 & b_{34} \\ 0 & 0 & b_{43} & 0 \end{bmatrix} \tag{16}$$

$$\mathcal{R}_d(x) = \begin{bmatrix} a_{11} & 0 & 0 & 0 \\ 0 & a_{22} & 0 & 0 \\ 0 & 0 & a_{33} & 0 \\ 0 & 0 & 0 & a_{44} \end{bmatrix} \tag{17}$$

$$b_{43} = -b_{34} = C_f O_{C21} \tag{18}$$

$$a_{11} = a_{22} = -L_f \xi_4 \tag{19}$$

$$a_{33} = a_{44} = -C_f O_{C11} = -C_f O_{C22} \tag{20}$$

$$H_d(x) = \frac{1}{2} L_f (i_{L\alpha} - i_{L\alpha ref})^2 + \frac{1}{2} L_f (i_{L\beta} - i_{L\beta ref})^2 + \frac{1}{2} C_f v_\alpha^2 + \frac{1}{2} C_f v_\beta^2. \tag{21}$$

III. Proposed Passivity-Based VOC Approach

A. Passivity-Based VOC Method in pH System

The control vectors *u* can then be solved, as given in (22), by matching the open-loop pH model in (9) and desired closed-loop pH model in (15). The detailed derivation process can be seen in Appendix B

$$u = \begin{bmatrix} u_\alpha \\ u_\beta \end{bmatrix} = \begin{bmatrix} -L_f \xi_4 (i_{L\alpha ref} - i_{L\alpha}) + R_f i_{L\alpha} + v_\alpha \\ -L_f \xi_4 (i_{L\beta ref} - i_{L\beta}) + R_f i_{L\beta} + v_\beta \end{bmatrix}. \tag{22}$$

Then, the passivity-based control theory can be applied to design the GFM to be stable with this control vector. The conventional passivity-based design is based on the interconnection damping assignment (IDA) approach [41], which is to design the closed-loop pH model in (15) to meet the following criteria:

1) $\mathcal{R}_d(x) = \mathcal{R}_d^T(x) \geq 0$ is positive semidefinite;
2) $\mathcal{J}_d(x) = -\mathcal{J}_d^T(x)$ is skew-symmetric;
3) $H_d(x)$ is a local minimum at desired equilibrium point $x*$.

However, the IDA approach is mainly intended for a fixed-point regulation or tracking of a reference, it does not meet the design goal in this article, which is to achieve a stable orbit. Therefore, for orbital stabilization, a modified IDA passivity-based approach via energy pumping and damping motion is adopted as follows [42].

First, the closed-loop Hamiltonian function $H_d(x)$ in (21) is decomposed into two parts: $H_l(x_l)$, as given in (23), which is to track the current reference following the conventional IDA approach and $H_p(x_p)$, as given in (24), which is to push the state trajectory to the desired orbit.

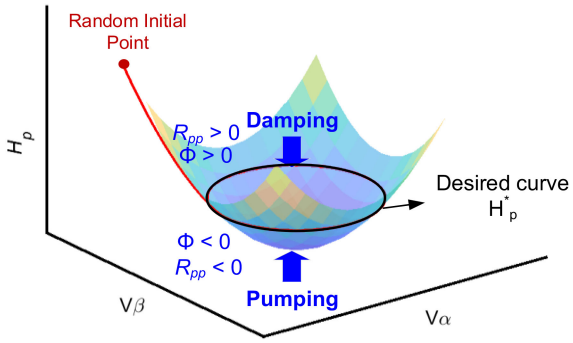

Fig. 2. Desired energy level H_p^* and closed orbit through energy pumping and damping motion.

Second, a function $\Phi(x_p)$ that defines the Jordan curve, a nonself-intersecting continuous loop in the plane is given in (25), with the desired capacitor energy level $H_p^* = \frac{1}{2}\, C_f(v_{\alpha ref}^2 + v_{\beta ref}^2) = \frac{1}{2}\, C_f v_{ref}^2 > \min(H_p(x_p))$.

Third, the damping matrix $\mathcal{R}_{\rm d}(\rm x)$ in (17) is reformatted as (26), where, $\mathcal{R}_{ll} = \left[\begin{smallmatrix} a_{11} & 0 \\ 0 & a_{22} \end{smallmatrix}\right]$, $\mathcal{R}_{pp} = \left[\begin{smallmatrix} a_{33} & 0 \\ 0 & a_{44} \end{smallmatrix}\right]$.

Then, as shown in Fig. 2, when H_p is larger than H_p^*, i.e., $\Phi(x_p) > 0$, the energy should be damped, i.e., $\mathcal{R}_{\rm pp} > 0$; when H_p is smaller than H_p^*, i.e., $\Phi(x_p) < 0$, more energy should be pumped into the system, i.e., $\mathcal{R}_{\rm pp} < 0$.

Therefore, with $\mathcal{R}_{\rm ll} > 0$and $\mathcal{R}_{\rm pp}$ satisfying the damping-and-pumping conditions in (27), the modified IDA passivity-based criteria can be obtained.

Note that several assumptions have been made to ensure that the system is asymptotically orbitally stable, including the following:

(H1) x_l^* is the largest invariant set in the set $\{x_l \in \mathbb{R}^{n-2} | \nabla^T H_l(x_l) \mathcal{R}_{ll}(x_l) \nabla H_l\,(x_l) = 0\}$;
(H2) $\mathcal{J}_d(x)$ satisfies $\nabla^T H_p(x_p) \mathcal{J}_{pl}\,(x) = 0$ and $\mathcal{J}_{(12)}\,(x) = \frac{c(x)}{\nabla x_0 H_{d0}(x_l, x_0)} \mid_{x_0 = \Phi(x_p)} \neq 0$, where $0 < |c(x)| < \infty$;
(H3) for some $\varepsilon_* > 0$ and ε_*-neighborhood $B_{\varepsilon_*}(x_p^*)$, $\nabla^2 H_p|_{x_p \in B_{\varepsilon_*}(x_p^*)} > 0$ and $\max_{B_{\varepsilon_*}(x_p^*)} H_p(x_p) > H_p^*$.

The assumptions H1 and H2 ensure that $\lim_{t\to\infty} x_l\,(t) = x_l^*$, which means the current can only converge to the reference current in the steady state; and the assumptions H2 and H3 guarantee that the voltage oscillator can only converge to the desired orbit

$$H_l\,(x_l) = \frac{1}{2}\, L_f (i_{L\alpha} - i_{L\alpha ref})^2 + \frac{1}{2} L_f (i_{L\beta} - i_{L\beta ref})^2 \quad (23)$$

$$H_p\,(x_p) = \frac{1}{2}\, C_f v_\alpha^2 + \frac{1}{2} C_f v_\beta^2 \quad (24)$$

$$\Phi\,(x_p) = H_p\,(x_p) - H_p^* \quad (25)$$

$$\mathcal{R}_d = \begin{bmatrix} \mathcal{R}_{ll_{2\times 2}} & 0_{2\times 2} \\ 0_{2\times 2} & \mathcal{R}_{pp_{2\times 2}} \end{bmatrix} \quad (26)$$

$$\mathcal{R}_{pp}\Phi \geq 0 \,\text{and}\, \mathcal{R}_{pp} = 0 \Leftrightarrow \Phi\,(x_p) = 0. \quad (27)$$

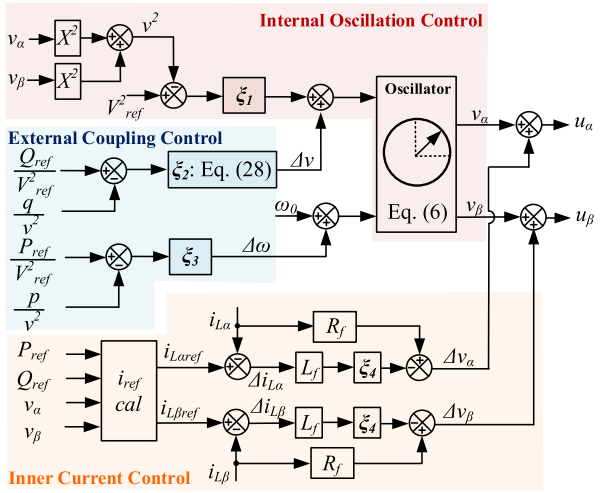

Fig. 3. Function blocks of the proposed passivity-based VOC method for GFMs.

B. Function Blocks of Proposed Control Approach

The detailed function blocks of the control vectors given in (22) can be found in Fig. 3. The control blocks consist of three parts: 1) external coupling control to determine the coupling strength between the inverter and the grid to achieve system synchronization through the active and reactive power regulation; 2) the internal oscillation control to mimic the virtual oscillator behavior of three-phase output voltage in $\alpha\beta 0$ frame; 3) the inner current control to provide damping for the current loop.

Applying the modified IDA passivity-based criterion to the design of parameters, the following three requirements can be obtained.

1) $b_{43} = -b_{34} \neq 0$. Also, ξ_3 should not be designed to be too large because the steady-state fundamental frequency of the inverter should be the same as the grid frequency so that the prespecified ac power flow solutions are still valid.
2) To achieve $\mathcal{R}_{\rm ll} > 0$, ξ_4 should be negative.
3) To meet the criterion in (27), the sign of ξ_2 should be adjusted following the rule in (28) and ξ_1 should be positive

$$sgn(\xi_2) = -sgn\left(\left(\frac{Q_{ref}}{v_{ref}^2} - \frac{Q}{v^2}\right)\left(v^2 - v_{ref}^2\right)\right). \quad (28)$$

As long as the control parameters are selected following the three requirements above, the GFMs will be GAS. It means that the GFM will autonomously synchronize with the rest of the grid under different scenarios, including grids with different SCRs, grids with large system disturbances, and grids with multiple inverters.

IV. Stability Analysis of Proposed Passivity-Based VOC Approach

A. Lyapunov Stability Analysis

To further validate that the GFMs with the proposed design are asymptotically stable, a Lyapunov energy function $V(x)$ can be constructed as (29) based on the Hamiltonian functions. First, it can be easily proven that $\mathrm{V}(x) > 0$ for $\forall x \neq x_{ref}$. Then, taking the time derivative of $V(x)$, (30) can then be obtained. According to $\mathcal{R}_{ll} > 0$ and (27), it can be concluded that $\dot{V}(x) < 0$ for $\forall x \neq x_{ref}$. Also, when $||x|| \to \infty,\ V(x) \to \infty$. Therefore, based on the properties of Lyapunov's second method and LaSalle's theorem, it is proven that the system is GAS in the region of attraction, which is defined as $\Omega = \{x \in R^n | \dot{V}(x) \leq 0\}$[25]

$$V\ (x) = H_l\ (x_l) + \frac{1}{2}\Phi^2\ (x_p) \tag{29}$$

$$\dot{V}\ (x) = \ -\nabla^T H_l R_{ll} \nabla H_l - \nabla^T H_p\ [R_{pp}\Phi]\ \nabla H_p. \tag{30}$$

Applying LaSalle's invariance principle, the state will ultimately converge into the largest invariant set $\mathcal{A}$ of the set $\{x \in R^n |\ x_l = x_l^*\ ,\ [R_{pp}(x)\Phi(x)]\nabla H_p(x) = 0\}$. It has been proven in [42] that $\mathcal{A} = \mathcal{C} \cup col(x_p^*, x_l^*)$ and $\mathcal{C}$ is a nonempty attractive closed orbit. That means if the GFM meets the modified IDA passivity-based criterion, it can eventually approach the desired voltage oscillator and current equilibrium points starting from any initial state.

B. Comparisons of Proposed Control Method With Existing Approaches

The stability of the proposed control approach has been mathematically analyzed based on the Lyapunov stability theorem in Section IV-A. It has been proved that the inverter can reach the steady-state operating point from any initial conditions due to the passivity-based control. To be more specific with the concept of power system stability, in this subsection, the synchronization stability will be investigated under the three scenarios introduced in Section I (i.e., SC1–SC3).

First of all, it has already been shown in [8] that the dVOC approaches are superior to the conventional droop control in terms of system synchronization stability. Therefore, the proposed approach will not be compared with conventional droop control and will only be compared with the more advanced dVOC approaches. Additionally, since the proposed control is developed based on the mechanism of coupled harmonic oscillators, it will have a similar structure as the existing dVOC approaches [4], [19], [20], [40]. Note that in the following discussion, the method in [19] and [40] will be denoted as dVOC1, the method in [4] and [20] will be denoted as dVOC2, and the proposed method will be denoted as PVOC. The circuit diagrams of system synchronization stability-related control blocks of dVOC1, dVOC2, and PVOC (ignoring the inner current loop in Fig. 3) can be obtained, respectively, as shown in Fig. 4, where the voltage oscillators are built based upon the line-to-line rms value of the output voltage.

The synchronization stability performance of the proposed PVOC can then be compared with the dVOC approaches.

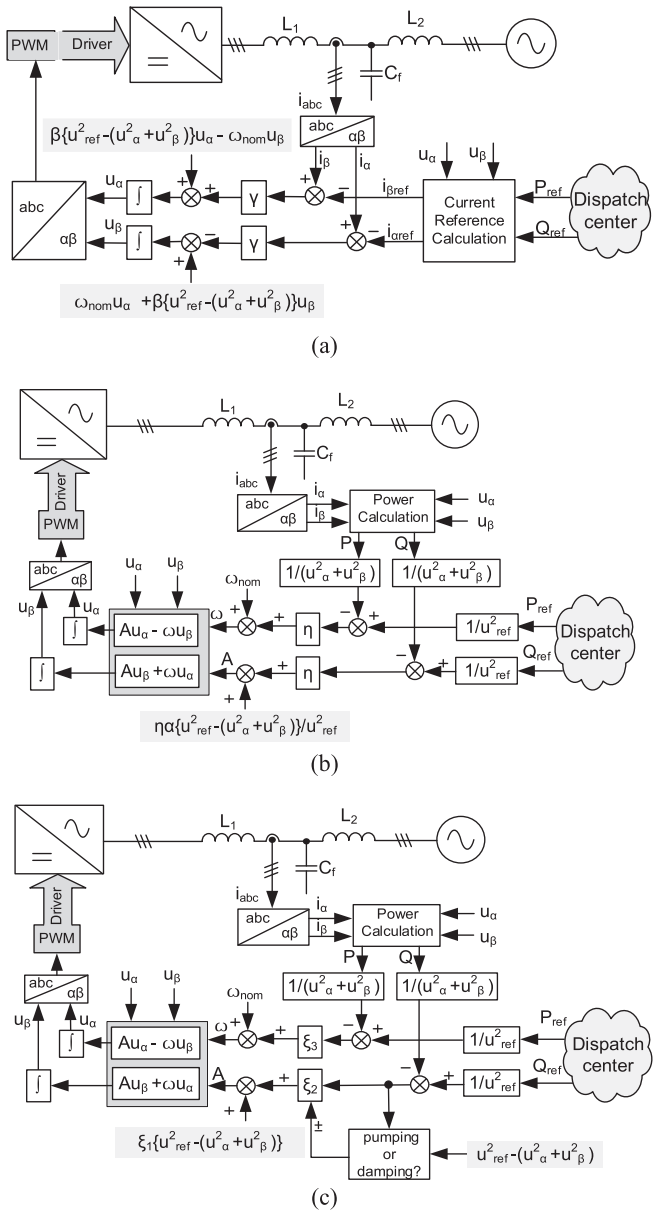

Fig. 4. Control diagrams of different VOC approaches. (a) dVOC1[19], [40]. (b) dVOC2 [4], [20]. (c) Proposed PVOC.

For SC1 and SC3, comparison results between the dVOC and the proposed approach can be easily obtained. First, for SC1, it has been proved in [8] that the dVOC approach will always remain stable as long as an equilibrium operating point exists with constant voltage amplitude. The same conclusion can be reached for the proposed control approach since if neglecting the voltage amplitude dynamics, the proposed PVOC would be the same as dVOC1 and dVOC2. Second, for SC3, the proposed approach is developed based on the theorem of passivity-based control design, so the stability of interconnection of multiple inverters can be guaranteed, while the control parameters of the dVOC approaches need to be designed with the system information.

While for SC2, a case study will be given below to illustrate the different performances between the proposed control and

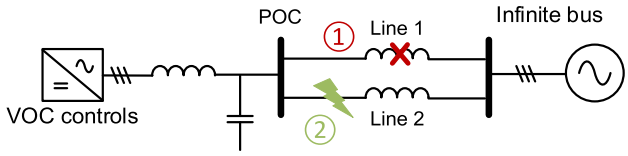

Fig. 5. Test scenarios of the transient stability analysis.

TABLE I
ELECTRICAL AND CONTROL PARAMETERS OF THE TEST SYSTEM

Variables		Value	Variables	Value
Output power		600 W/1 p.u.	Peak phase voltage	40.8 V/1 p.u.
Dc voltage		130 V	Switching frequency	10 kHz
System frequency		60 Hz	Line 1	6 mH/0.54 p.u.
Output inductance		2.4 mH/ 0.22 p.u.	Line 2	6 mH/0.54 p.u.
Power droop gain		$\gamma = \eta = \lvert\xi_2\rvert = \xi_3 = 15$		
Oscillator convergence speed	Fast	$\beta = \xi_1 = \frac{\eta\alpha}{u_{ref}^2} = 0.02$		
	Slow	$\beta = \xi_1 = \frac{\eta\alpha}{u_{ref}^2} = 0.001$		

the existing dVOC approaches. A system of a GFM connected to an infinite bus through two paralleled transmission lines, as shown in Fig. 5, is adopted as an example for a comparison study of system transient stability. Two fault scenarios will be considered, including the following:

1) open-circuit fault (OCF) on Line 1;
2) short-circuit fault (SCF) with $L_{\text{short}} = 1$ mH on Line 2.

More specifically, for the OCF, it is assumed that the fault happens at 4 s, during fault there is an equilibrium point, and the fault will be cleared by restoring Line 1 at 8 s. For the SCF, it is assumed that the fault happens at 2 s, during fault there is no equilibrium point, and the fault will be cleared by disconnecting Line 2 after 250 ms.

To achieve a fair comparison, the control parameters of the three methods are designed to be equivalent. Also, two groups of control parameters considering different voltage oscillator convergence speeds are investigated, including a fast- and a slow- oscillator convergence speed. A larger value of β, α, or ξ_1 means a faster voltage convergence speed [19]. The detailed electrical and control parameters of the test system are given in Table I.

The dynamic equations for the three VOC approaches can be obtained for the system transient stability analysis. The frequency and voltage dynamic equations for dVOC1 can be obtained as (31) and the equations for dVOC2 are given in (32), where γ and η are the power control gains, β and α are oscillator convergence speed. For the proposed method, the current loop has almost no impact on system transient stability due to its small control gain and thus can be neglected. The frequency and voltage dynamic equations for PVOC can then be obtained as (33), where ξ_1 is the oscillator convergence speed, ξ_2 and ξ_3 are the power loop control parameters. Note that u in these equations is the control voltage, not the output voltage of the inverter. Also, assume that the cut-off frequency of the LPFs in the measured power signals is large enough, so their impacts can be neglected for the transient stability analysis here

$$\begin{cases} \dot{\delta} = \frac{\gamma}{u^2} \left\{P_{ref} - P\left(u\right)\sin\delta\right\} \\ \dot{u} = \beta\left(u_{ref}^2 - u^2\right)u + \frac{\gamma}{u}\left\{Q_{ref} - Q\left(u,\delta\right)\right\} \end{cases} \tag{31}$$

$$\begin{cases} \dot{\delta} = \eta\left(\frac{P_{ref}}{u_{ref}^2} - \frac{P(u)\sin\delta}{u^2}\right) \\ \dot{u} = \frac{\eta\alpha}{u_{ref}^2}\left(u_{ref}^2 - u^2\right)u + \eta\left(\frac{Q_{ref}}{u_{ref}^2} - \frac{Q(u,\delta)}{u^2}\right)u \end{cases} \tag{32}$$

$$\begin{cases} \dot{\delta} = \xi_3\left(\frac{P_{ref}}{u_{ref}^2} - \frac{P(u)\sin\delta}{u^2}\right) \\ \dot{u} = \xi_1\left(u_{ref}^2 - u^2\right)u + \xi_2\left(\frac{Q_{ref}}{u_{ref}^2} - \frac{Q(u,\delta)}{u^2}\right)u \end{cases}. \tag{33}$$

To analyze the system transient stability, these two coupled dynamic equations in (31)–(33) will be numerically solved using the MATLAB command "ode45" with which the phase portrait $\dot{\delta} - \delta$ and $u - \delta$ curve can be plotted, then the time-domain simulation results will be obtained to further verify the analysis results.

1) Transient Stability Under Different Fault Conditions:

Case 1: Fast convergence speed under OCF

In Case I with the OCF on Line 1 and with the fast convergence speed of the oscillator control, it can be seen from Fig. 6 that the system with all three control methods can reach a steady-state operating point before the fault occurs (i.e., $\dot{\delta} = 0$ in phase portrait) from a random initial point, during the fault, and after the fault is cleared, separately. Also, since the fault is cleared by restoring Line 1, the system will return to the same operating point as the prefault condition after the fault is cleared. Additionally, it can be noticed that the PVOC has better control voltage regulation capability (i.e., $u = 1$ p.u.) than the other two approaches.

Case 2: Slow convergence speed under OCF

In Case 2 with the OCF on Line 1 and with a slow convergence speed of the oscillator control, it can be seen from Fig. 7 that the system with dVOC2 and PVOC can reach a steady-state operating point before the fault occurs, during the fault and after the fault is cleared, separately. However, the system with dVOC1 loses synchronism during fault and cannot return to steady-state conditions after the fault is cleared because of the sharp voltage drop. Additionally, the proposed PVOC has better voltage and power regulation capability than dVOC2.

Case 3: Fast convergence speed under SCF

In Case 3 with the SCF on Line 2 and with the fast convergence speed of the oscillator control, it can be seen from Fig. 8 that the system with all the three control methods can reach a steady-state operating point before the fault occurs and after the fault is cleared, separately. And during the fault, since no equilibrium point exists, none of the three methods can reach a steady state. In addition, the fault is cleared by disconnecting Line 2, so the system will return to another operating point after the fault is cleared. Additionally, it can also be noticed that the PVOC

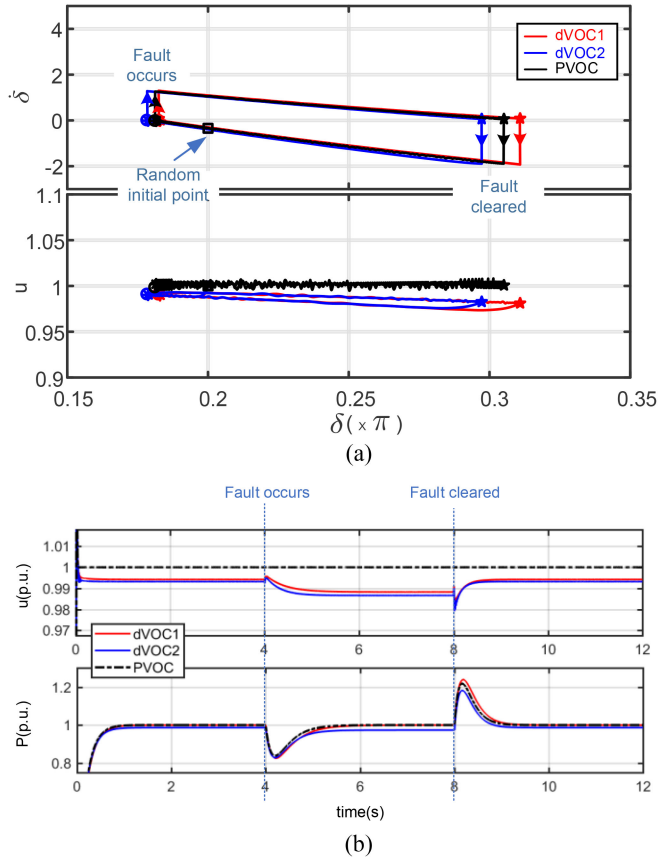

Fig. 6. Case I: (a) analysis result and (b) simulation result.

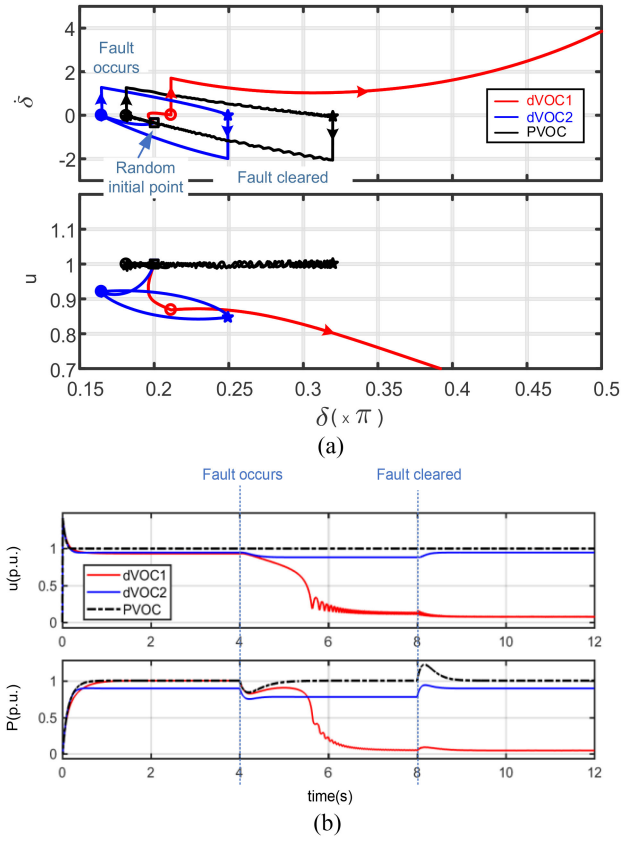

Fig. 7. Case 2: (a) analysis result and (b) simulation result.

approach has better voltage regulation capability than the other two approaches.

Case 4: Slow convergence speed under SCF

In Case 4 with the SCF on Line 2 and with a slow convergence speed of the oscillator control, it can be seen from Fig. 9 that the system with both dVOC2 and PVOC can reach a steady-state operating point before the fault occurs and after the fault is cleared, separately. And during the fault, since no equilibrium point exists, neither of the two methods can reach a steady state. In addition, the fault is cleared by disconnecting Line 2, so the system will return to another operating point after the fault is cleared. Additionally, it can be noticed that PVOC has better voltage regulation and power regulation capability than dVOC2. While the system with dVOC1 will lose synchronism during fault and cannot return to a steady state after the fault is cleared due to the sharp voltage drop.

2) Impacts of LPFs in Power Loops on System Stability: From the results abovementioned, it can be concluded that dVOC1 has worse stability performance than dVOC2 and PVOC. In addition, dVOC2 has poorer voltage and power regulation capability than PVOC.

In this section, stability comparisons will be continued between dVOC2 and PVOC with considering the LPFs in the power measurement loops when the cut-off frequency is low. Normally,

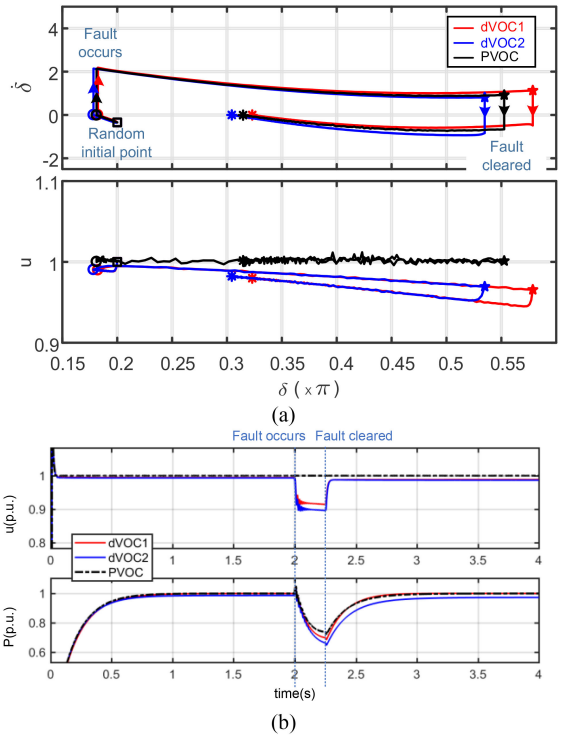

Fig. 8. Case 3: (a) analysis result and (b) simulation result.

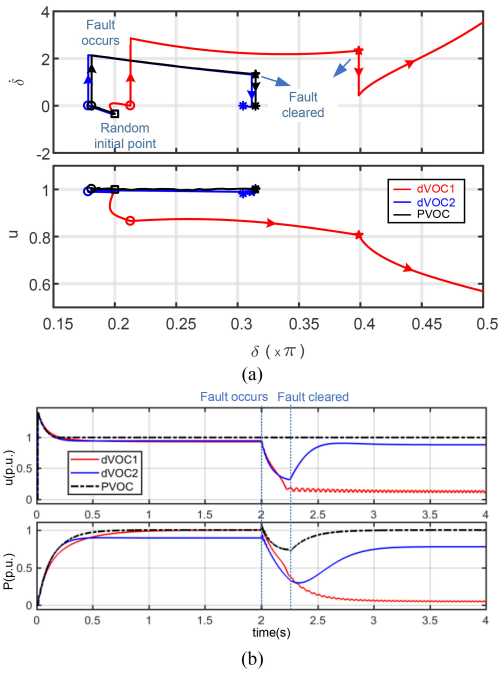

Fig. 9. Case 4: (a) analysis result and (b) simulation result.

an LPF will be added to filter out the noises in the measured power in the system. So, the phase and voltage dynamics of dVOC2 and PVOC can be modified as (34) and (35), separately, where ω_{LPF} is the cut-off frequency of the LPF and s is the Laplace operator

$$\begin{cases} \dot{\delta} = \eta \left(\frac{P_{ref}}{u_{ref}^2} - \frac{\omega_{\text{LPF}}}{s+\omega_{\text{LPF}}} \frac{P(u)\sin\delta}{u^2} \right) \\ \dot{u} = \frac{\eta\alpha}{u_{ref}^2} \left(u_{ref}^2 - u^2 \right) u + \eta \left(\frac{Q_{ref}}{u_{ref}^2} - \frac{\omega_{\text{LPF}}}{s+\omega_{\text{LPF}}} \frac{Q(u,\delta)}{u^2} \right) u \end{cases} \tag{34}$$

$$\begin{cases} \dot{\delta} = \xi_3 \left(\frac{P_{ref}}{u_{ref}^2} - \frac{\omega_{\text{LPF}}}{s+\omega_{\text{LPF}}} \frac{P(u)\sin\delta}{u^2} \right) \\ \dot{u} = \xi_1 \left(u_{ref}^2 - u^2 \right) u + \xi_2 \left(\frac{Q_{ref}}{u_{ref}^2} - \frac{\omega_{\text{LPF}}}{s+\omega_{\text{LPF}}} \frac{Q(u,\delta)}{u^2} \right) u \end{cases} . \tag{35}$$

The system transient stability will be analyzed under Case 4 where there is a short-circuit fault on Line 2 with slow oscillator voltage convergence speed. The cut-off frequency of the LPFs that are added in both active power and reactive power loops is 1 Hz. Fig. 10 shows the simulation results of the transient stability with dVOC2 and PVOC. Since it is difficult to solve the dynamic equations in (34) and (35) directly, the $\dot{\delta} - u - \delta$ will be drawn based on the simulation results instead. From the simulation results, it can be observed that dVOC2 will lose synchronism when the fault occurs and cannot return to steady-state operating conditions after the fault is cleared due to the sharp voltage drop when LPFs are added to the power measurement loops. It has also been found that impacts of the two LPFs in the active power and reactive power loop of dVOC2 are unlike those in the conventional active power-frequency (p-f) and reactive power-voltage (Q-v) droop control. Pan *et al.* [43] concluded that the slow LPF in the p-f droop control loop will

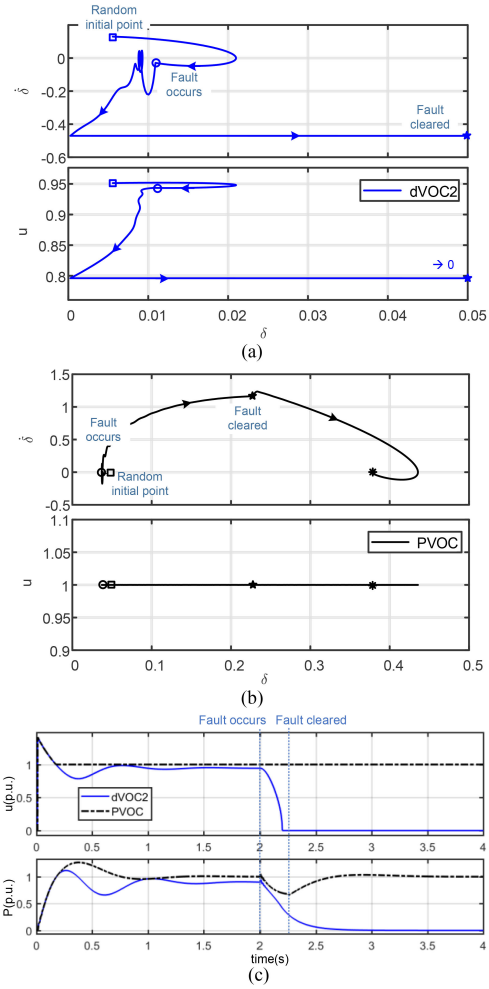

Fig. 10. Simulation results of transient stability under SCF with fast convergence speed and LPFs in power measurement loop: (a) $\dot{\delta} - u - \delta$ curve of dVOC2, (b) $\dot{\delta} - u - \delta$ curve of PVOC, and (c) time-domain simulation.

degrade the system stability, while the slow LPF in Q-v droop control loop can improve the system stability. However, for the dVOC2 approaches, it has been found that the LPF in the active power loop does not affect system stability, while the LPF in the reactive power loop will affect system transient stability. That is, a slow LPF with a low cut-off frequency of reactive power loop can exacerbate the system transient stability. However, LPFs in the power loops of the proposed PVOC will not affect system transient stability because of the good voltage regulation capability provided by the pumping-and-damping motion in the reactive power loop.

So far, stability comparisons among the existing control strategies and the proposed control method considering the scenarios introduced in Section I (SC1–SC3) can be obtained, as shown in Table II.

V. Parameter Design of Proposed Control Considering Dynamic Requirements

In addition to the limitations of IDA passivity-based design criteria on the selection of control parameters, the dynamic

TABLE II
STABILITY COMPARISONS OF DIFFERENT CONTROL STRATEGIES

Control methods	SC1: Is the system small-signal stable under different SCRs?	SC2: Transient stability?	SC3: Is system information required for control design?
Droop control w/o LPF [43]	Stable	Heavily damped *p-f* droop, but *Q-v* droop may worsen system stability by causing a voltage drop	Yes
Droop control with LPF or VSM [8], [43], [44]	Might be unstable under stiff grid conditions due to less damping	Second-order frequency dynamics like power swing dynamics of SGs and *Q-v* droop may worsen its stability by causing a voltage drop	Yes
dVOC [8]	Stable	Same as droop control w/o LPF	Yes
Proposed PVOC	Stable	Stable	No

TABLE III
WORKING CONDITIONS AND CONTROL PARAMETERS OF THE SINGLE-INVERTER TEST

Variables	Value	Variables	Value
Dc voltage (V)	130	Grid impedance L_g (mH)	3.6 (0.54 p.u.)
Ac voltage (V)	50	Voltage rising time T_{rise} (ms)	20
Power references P_{ref}, Q_{ref} (kW, kvar)	0.6, 0	Control variable ξ_1	0.0605
Rated power S_{rated} (kVA)	1	Control variable $\lvert\xi_2\rvert$	0.42
Output inductor L_f (mH)	2.4 (0.36 p.u.)	Control variable ξ_3	31.4
Output capacitor C_f (μF)	10	Control variable ξ_4	-20

TABLE IV
WORKING CONDITIONS AND PER UNIT VALUE OF SYSTEM PARAMETERS IN MULTIPLE INVERTER TEST

Variables	Value	Variables	Value
Dc voltage (V)	130	Line 1 (p.u.)	0.37
Ac voltage (V)	50	Line 2(p.u.)	0.18 → 0.54
Rated power (kVA)	1	Line 3 (p.u.)	0.11 → 0.47
Real power of G_{12} (p.u.)	0.2 → 0.8 → -0.2	Line 4(p.u.)	0.38
Real power of G_{13} (p.u.)	0.5	Line 5 (p.u.)	0.11
Real power of G_{22} (p.u.)	0.5	Line 6(p.u.)	0.11
Real power of G_{23} (p.u.)	0.5	Line 7 (p.u.)	0.11

response of the inverter should also be considered. Therefore, several tips on the control parameter design are given as follows. Note that the calculated values will be used in the simulation and experimental analysis in Section VI.

A. Inner Voltage Oscillator Dynamics

By ignoring the slower power dynamics in (6), the voltage dynamics equation can be derived as (36). Then, the time of voltage rising from $k_1 V_{ref}$ to $k_2 V_{ref}$ can be calculated based on (37). Therefore, with the specification on voltage rising time t,

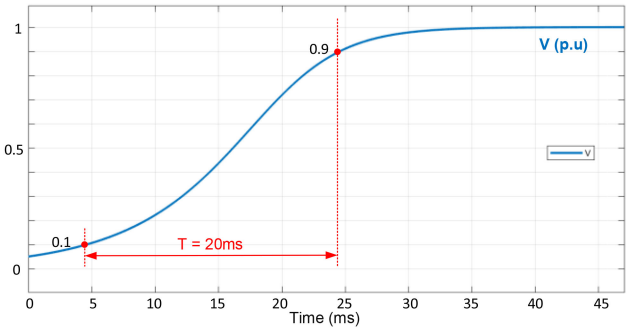

Fig. 11. Voltage rising time with designed ξ_1.

ξ_1 can be determined [19]

$$\dot{v} = \xi_1 \left(v_{ref}^2 - |v|^2 \right) v \tag{36}$$

$$t = \frac{1}{2\xi_1 v_{ref}^2} ln \left(\frac{k_2^2 \left(k_1^2 - 1\right)}{k_1^2 \left(k_2^2 - 1\right)} \right). \tag{37}$$

For example, if the time of voltage rising from 0.1 V_{ref} to 0.9 V_{ref} is 20 ms, then, ξ_1 is calculated to be 0.0605 with V_{ref} = 50 V based on (37). The voltage rising time of the voltage vector with designed ξ_1 can be seen in Fig. 11.

B. Power Dynamics

Taking power dynamics into consideration, the system is then expressed as (38). For simplicity, the dynamics of a faster inner voltage loop are ignored, therefore, the system dynamics can be simplified as (39). It can be observed from (39) that the power dynamics of the proposed control are similar to conventional droop control, as shown in (40) if the voltage dynamics are ignored. In the field application, the selection of the *P-f* droop gain *m* and *Q-v* droop gain *n* are usually designed to be several percentages (k_q and k_p) of the nominal value as $n = k_q \frac{V_{ref}}{P_{ref}}$ and $m = k_p \frac{\omega_R}{P_{ref}}$. Therefore, mapping from the proposed control to droop control, the outer coupling term gains care suggested to design as $|\xi_2| = k_q \frac{V_{ref}^2}{P_{ref}}$ and $\xi_3 = k_p \frac{\omega_R V_{ref}^2}{P_{ref}}$. For example, $k_p = 2\%$, $k_q = 10\%$, so $\xi_3 = 31.4$, $|\xi_2| = 0.42$. Note that ξ_2 is a sign-indefinite value in the proposed control, the absolute

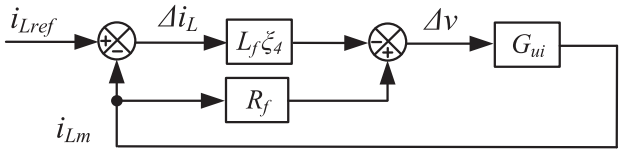

Fig. 12. Equivalent circuit of the inner current loop.

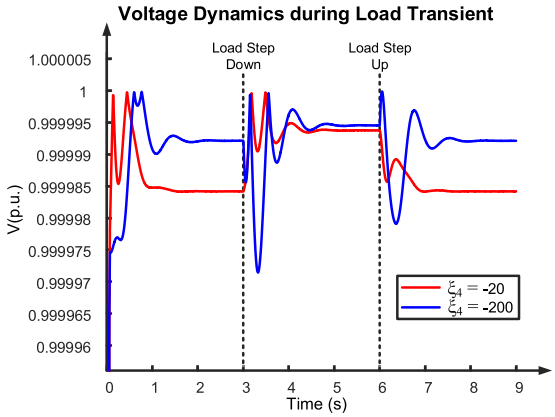

Fig. 13. Voltage dynamics under load transient with different ξ_4.

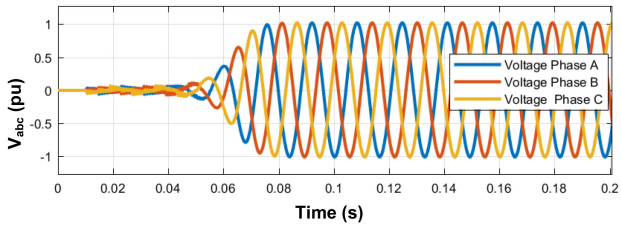

Fig. 14. Start-up of the GFM with the proposed passivity-based VOC method.

value is considered here for simplicity

$$\begin{cases} \dot{V} = \xi_1 \left(V_{ref}^2 - |V|^2\right) V + \xi_2 \left(\frac{Q_{ref}}{V_{ref}^2} - \frac{Q_m}{V^2}\right) v \\ \dot{\theta} = \omega_R + \xi_3 \left(\frac{P_{ref}}{V_{ref}^2} - \frac{P_m}{V^2}\right) \end{cases} \tag{38}$$

$$\begin{cases} \dot{V} = V_{ref} + \frac{\xi_2}{V_{ref}} \left(Q_{ref} - Q_m\right) \\ \dot{\theta} = \omega_R + \frac{\xi_3}{V_{ref}^2} \left(P_{ref} - P_m\right) \end{cases} \tag{39}$$

$$\begin{cases} \dot{V} = V_{ref} + n \left(Q_{ref} - Q_m\right) \\ \dot{\theta} = \omega_R + m \left(P_{ref} - P_m\right). \end{cases} \tag{40}$$

C. Inner Current Loop Control Dynamics

The inner current dynamics have the least impact on system stability if $\xi_4 < 0$, but it may have some impact on system load transient performance. To have a control parameter design of the inner current loop, the equivalent circuit is obtained, as shown in Fig. 12. Then, the model of the inner current loop can be derived as (41), where $G_{ui} = \frac{sC_f}{(sL_f+R_f)sC_f+1}$. To have faster voltage transient, ξ_4 should be designed to cause small Δv following equations in (42) as follows:

$$T_i = -G_{ui} \left(L_f \xi_4 + R_f\right) \tag{41}$$

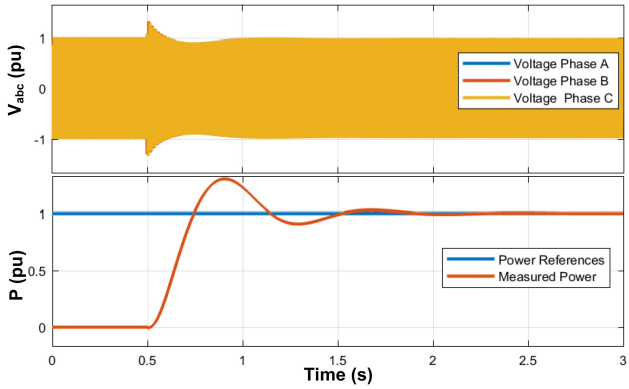

Fig. 15. Stable connection of the GFM with the proposed passivity-based VOC method into the grid.

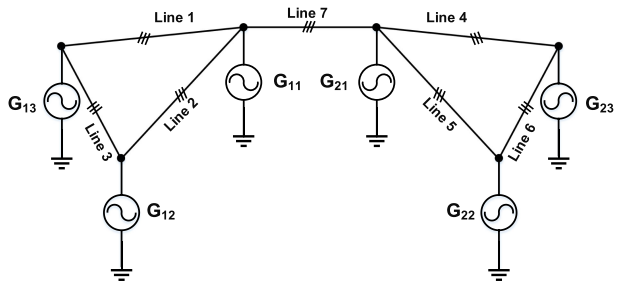

Fig. 16. Circuit diagram of the six-inverter system test with the proposed control method.

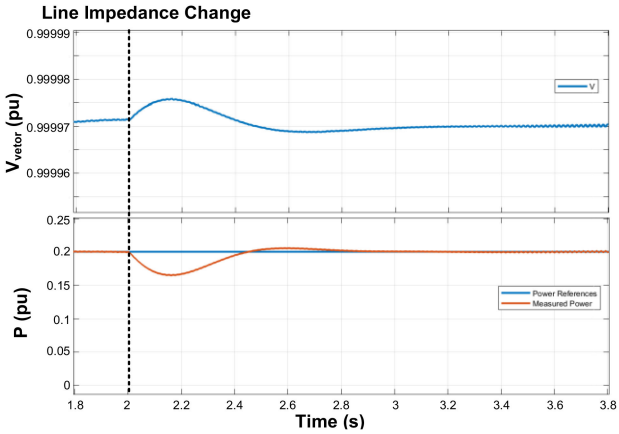

Fig. 17. Simulation results of G_{12} when the system line impedance changes during an out-of-service fault.

$$\Delta v = \frac{-L_f \xi_4 i_{Lref}}{1 + T_i}. \tag{42}$$

For example, with different ξ_4 values, the system exhibits different voltage dynamics though the differences are small. As shown in Fig. 13, ξ_4 is preferred to be selected as -20 to have a better load transient.

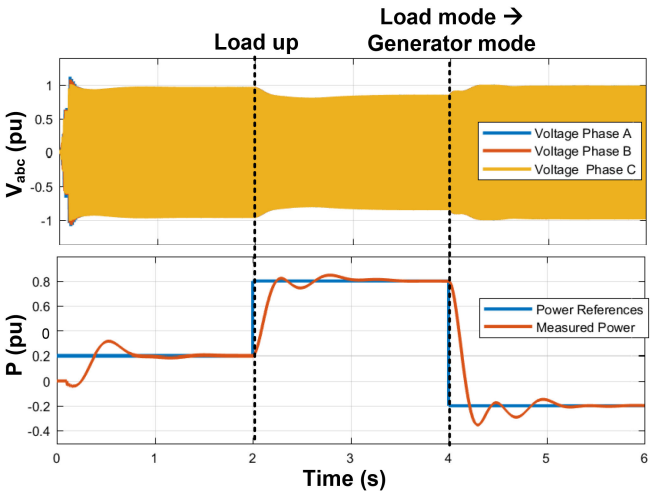

Fig. 18. Simulation results with load power change at G_{12}.

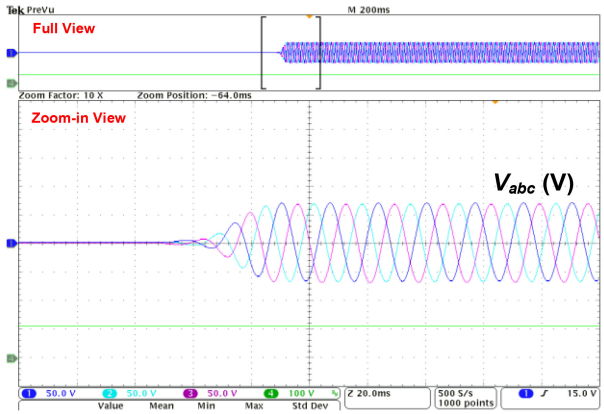

Fig. 19. Voltages at PCC during start-up of the GFM with the proposed control method in islanded mode.

VI. Simulation and Experimental Validation

A. Simulation Testing

To validate the effectiveness of the proposed control method, several scenarios are simulated and examined in MATLAB/Simulink, including systems with a single GFM and with multiple GFMs.

1) Stable Operation of a Single GFM With the Proposed Method: In the single-inverter test, both the islanded mode and grid-connected mode are considered. The control parameters and working conditions are listed in Table III.

Fig. 14 shows that the proposed control method can start up properly in the islanded mode. Also, in the grid-connected mode, the inverter can be connected to the grid smoothly, as shown in Fig. 15 at $t = 0.5$ s.

2) Stable Operation of Multiple GFMs With the Proposed Control: A system with six inverters that are implemented with the proposed control approaches, as shown in Fig. 16, is built in MATLAB/Simulink for further validation under two transient scenarios: I) change of line impedances and II) change of load power. The working conditions and system parameters are listed in Table IV.

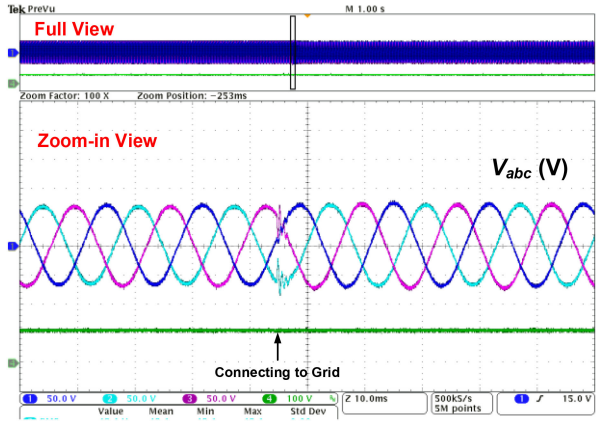

Fig. 20. Voltages at PCC in a stable connection of the GFM into the grid in grid-connected mode.

Fig. 21. HTB of the six-inverter system test with the proposed control method.

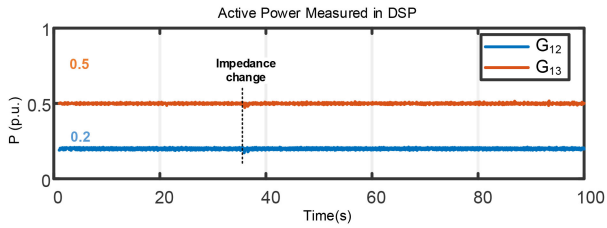

Fig. 22. Measured power of G_{12} and G_{13} when system line impedance changes during an out-of-service fault.

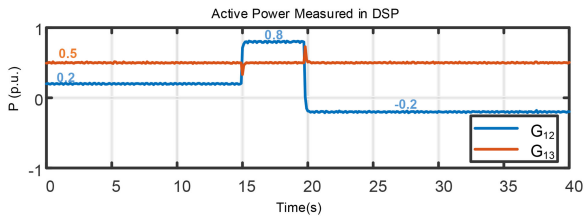

Fig. 23. Measured power of G_{12} and G_{13} with load power change.

Scenario I: Change of Line Impedance

In this scenario, the impedances of Line 2 and Line 3 are assumed to be increased to emulate some out-of-service faults.

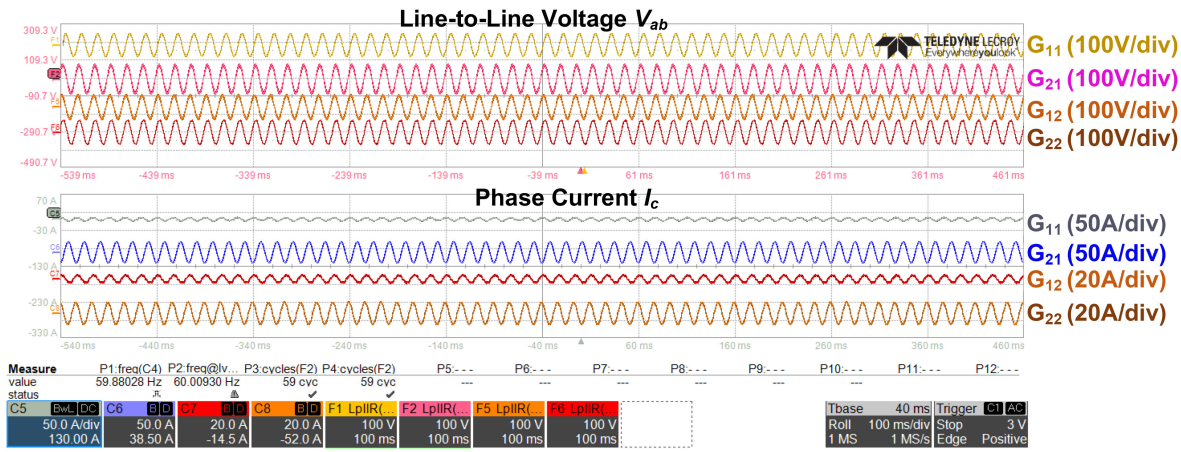

Fig. 24. Measured voltage and current waveforms when system line impedance changes under an out-of-service fault.

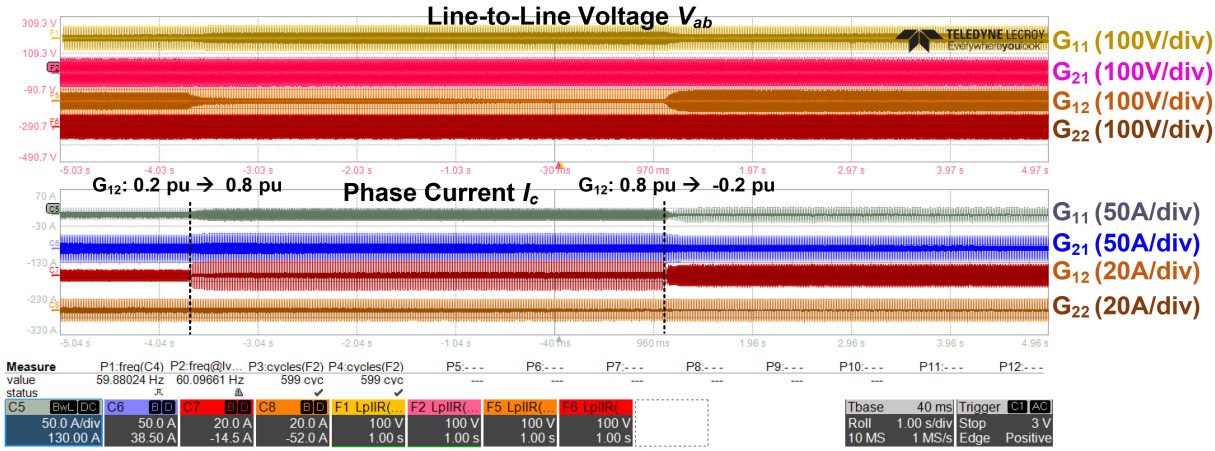

Fig. 25. Measured voltage and current waveforms with load power change.

It can be seen from Fig. 17 that the change of line impedances at $t = 2$ s will not affect system stability, both the voltage and power will return to a stable value after the transient.

Scenario II: Change of Load Power

In this scenario, the power of G_{12} is assumed to change from 0.2–0.8 p.u. at $t = 2$ s and then to -0.2 p.u. at $t = 4$ s. Note that the positive power means the inverter is a load that is consuming power in the system, and the negative power means the inverter is a source that is providing power to the system. As shown in Fig. 18, during the load transient, the voltage can be kept stable, and the power can track the references well.

B. Experimental Testing

1) Stable Operation of a Single GFM With the Proposed ASC Method: An experimental setup of the single GFM is built to verify the effectiveness of the proposed passive control strategy with the same parameters as listed in Table III. Figs. 19 and 20 show that the system is stable in both islanded mode and grid-connected mode.

2) Stable Operation of Multiple Inverters With the Proposed Control: The six-inverter system with the proposed control is tested with NSF/DOE CURENT hardware testbed (HTB) [45], as shown in Fig. 21. The proposed control method is implemented on the DSPs (TMS320F28335) for local control of each inverter. The working conditions and system parameters are the same as given in Table IV, and the control parameters of each inverter are given in Table III.

Scenario I: Change of Line Impedance

The system is tested under different line impedance values with Line 2 changing from 0.18–0.54 p.u. and Line 3 changing from 0.11–0.47 p.u. It can be seen from Figs. 22 and 24 that the system can remain stable under different grid network conditions.

Scenario II: Change of Load Power

When the load power changes, for example, the real power of G_{12} is changed from 0.2 p.u. to 0.8 p.u. to -0.2 p.u., it can be seen from Figs. 23 and 25 that the system is stable no matter how the load conditions are.

VII. Conclusion

To develop a grid-forming inverter with the capability of maintaining synchronization stability under different grid conditions without the need for the knowledge of grid dynamics, a passivity-based port-Hamiltonian system theory with a general VOC approach has been proposed. First, an energy-based model in the port-Hamiltonian framework for GFMs is developed, with the closed-loop behavior to mimic the coupled SL harmonic oscillators. The inverter is proved to be global asymptotic stable with the positive damping of the inductor current and the energy pumping and damping of the capacitor voltage. In addition to the stability requirements, the dynamic performance of GFMs is also considered for the control parameter design. Simulation and experimental results are given to validate the effectiveness of the proposed control method.

The method assumes a grid that is global asymptotic stable from any initial states. The future work is to extend the proposed method to a more general system.

Appendix A
Coupling Strength Derivation

Normally for coupled oscillators, the synchronization is achieved by adjusting the coupling strength γ and μ. However, in power systems, the coupling strength is fixed, which is defined by the connecting line parameters. The system synchronization is then obtained by achieving the predefined steady-state working conditions, i.e., P_{ref} and Q_{ref}

$$\begin{aligned}\begin{bmatrix} CP_\alpha \\ CP_\beta \end{bmatrix} &= \begin{bmatrix} \gamma\left(v_{\alpha g}-v_\alpha\right)-\mu\left(v_{\beta g}-v_\beta\right) \\ \gamma\left(v_{\beta g}-v_\beta\right)+\mu\left(v_{\alpha g}-v_\alpha\right) \end{bmatrix} \\ &= \begin{bmatrix} -\gamma & \mu \\ -\mu & -\gamma \end{bmatrix}\begin{bmatrix} v_\alpha \\ v_\beta \end{bmatrix}+\begin{bmatrix} \gamma & -\mu \\ \mu & \gamma \end{bmatrix}\begin{bmatrix} v_{\alpha g} \\ v_{\beta g} \end{bmatrix}. \end{aligned} \tag{A.1}$$

In the steady state, the instantaneous power flowing out of the inverter to the grid can be calculated, as (A.2) and (A.3), where $\delta = \theta_g - \theta$

$$\begin{aligned} P_{ref} &= \frac{v^2R - vv_g\left[R\cos\left(\delta\right)+\omega_oL_g\sin\left(\delta\right)\right]}{R^2+\left(\omega_oL_g\right)^2} \\ &= \mu v^2 - vv_g\left[\mu\cos\left(\delta\right)+\gamma\sin\left(\delta\right)\right] \end{aligned} \tag{A.2}$$

$$\begin{aligned} Q_{ref} &= \frac{v^2\omega L_g - vv_g\left[\omega_oL_g\cos\left(\delta\right)-R\sin\left(\delta\right)\right]}{R^2+\left(\omega_oL_g\right)^2} \\ &= \gamma v^2 - vv_g\left[\gamma\cos\left(\delta\right)-\mu\sin\left(\delta\right)\right] \end{aligned} \tag{A.3}$$

Therefore,

$$\mu\cos\left(\delta\right)+\gamma\sin\left(\delta\right) = \frac{\mu v^2 - P_{ref}}{vv_g} \tag{A.4}$$

$$\gamma\cos\left(\delta\right)-\mu\sin\left(\delta\right) = \frac{\gamma v^2 - Q_{ref}}{vv_g}. \tag{A.5}$$

Assuming $v_g = v + \Delta v$, $v_{\alpha g} = v_g \cos\theta_g$ and $v_{\beta g} = v_g \sin\theta_g$, and according to $\theta_g = \theta + \delta$

$$\begin{aligned}\begin{bmatrix} \gamma & -\mu \\ \mu & \gamma \end{bmatrix}\begin{bmatrix} v_{\alpha g} \\ v_{\beta g} \end{bmatrix} &= \begin{bmatrix} \gamma & -\mu \\ \mu & \gamma \end{bmatrix}\begin{bmatrix} v_g\cos\theta_g \\ v_g\sin\theta_g \end{bmatrix} \\ &= \begin{bmatrix} \gamma & -\mu \\ \mu & \gamma \end{bmatrix}\begin{bmatrix} \cos\delta & -\sin\delta \\ \sin\delta & \cos\delta \end{bmatrix}\begin{bmatrix} v_\alpha+\Delta_{v\alpha} \\ v_\beta+\Delta_{v\beta} \end{bmatrix} \\ &= \begin{bmatrix} \gamma\cos\delta-\mu\sin\delta & -\gamma\sin\delta-\mu\cos\delta \\ \gamma\sin\delta+\mu\cos\delta & \gamma\cos\delta-\mu\sin\delta \end{bmatrix}\begin{bmatrix} v_\alpha \\ v_\beta \end{bmatrix}\frac{v_g}{v}. \end{aligned} \tag{A.6}$$

Substituting (A.4)–(A.7) can be obtained

$$\begin{aligned}\begin{bmatrix} \gamma & -\mu \\ \mu & \gamma \end{bmatrix}\begin{bmatrix} v_{\alpha g} \\ v_{\beta g} \end{bmatrix} &= \begin{bmatrix} \frac{\gamma v^2 - Q_{ref}}{vv_g} & -\frac{\mu v^2 - P_{ref}}{vv_g} \\ \frac{\mu v^2 - P_{ref}}{vv_g} & \frac{\gamma v^2 - Q_{ref}}{vv_g} \end{bmatrix}\begin{bmatrix} v_\alpha \\ v_\beta \end{bmatrix}\frac{v_g}{v} \\ &= \begin{bmatrix} \gamma - \frac{Q_{ref}}{v^2} & -\mu + \frac{P_{ref}}{v^2} \\ \mu - \frac{P_{ref}}{v^2} & \gamma - \frac{Q_{ref}}{v^2} \end{bmatrix}\begin{bmatrix} v_\alpha \\ v_\beta \end{bmatrix}. \end{aligned} \tag{A.7}$$

Therefore, the coupling term under a steady state can be modeled as

$$\begin{bmatrix} CP_{\alpha,ref} \\ CP_{\beta,ref} \end{bmatrix} = \begin{bmatrix} -\gamma & \mu \\ -\mu & -\gamma \end{bmatrix}\begin{bmatrix} v_\alpha \\ v_\beta \end{bmatrix}+\begin{bmatrix} \gamma-\frac{Q_{ref}}{v^2} & -\mu+\frac{P_{ref}}{v^2} \\ \mu-\frac{P_{ref}}{v^2} & \gamma-\frac{Q_{ref}}{v^2} \end{bmatrix}$$

$$\begin{bmatrix} v_\alpha v_\beta \end{bmatrix} = \begin{bmatrix} -\frac{Q_{ref}}{v^2} & \frac{P_{ref}}{v^2} \\ -\frac{P_{ref}}{v^2} & -\frac{Q_{ref}}{v^2} \end{bmatrix}\begin{bmatrix} v_\alpha \\ v_\beta \end{bmatrix}. \tag{A.8}$$

Appendix B
Solving Control Vectors Through the Matching Equation

By matching (9) and (15), (B.1) can be obtained as

$$\begin{aligned} \dot{x} &= \left(\begin{bmatrix} 0 & 0 & -1 & 0 \\ 0 & 0 & 0 & -1 \\ 1 & 0 & 0 & 0 \\ 0 & 1 & 0 & 0 \end{bmatrix}-\begin{bmatrix} R_f & 0 & 0 & 0 \\ 0 & R_f & 0 & 0 \\ 0 & 0 & 0 & 0 \\ 0 & 0 & 0 & 0 \end{bmatrix}\right)\begin{bmatrix} i_{L\alpha} \\ i_{L\beta} \\ v_\alpha \\ v_\beta \end{bmatrix} \\ &+\begin{bmatrix} 1 & 0 \\ 0 & 1 \\ 0 & 0 \\ 0 & 0 \end{bmatrix}\begin{bmatrix} u_\alpha \\ u_\beta \end{bmatrix}-\begin{bmatrix} 0 & 0 \\ 0 & 0 \\ 1 & 0 \\ 0 & 1 \end{bmatrix}\begin{bmatrix} i_{g\alpha} \\ i_{g\beta} \end{bmatrix} \\ &= \left(\begin{bmatrix} 0 & 0 & 0 & 0 \\ 0 & 0 & 0 & 0 \\ 0 & 0 & 0 & b_{34} \\ 0 & 0 & b_{43} & 0 \end{bmatrix}-\begin{bmatrix} a_{11} & 0 & 0 & 0 \\ 0 & a_{22} & 0 & 0 \\ 0 & 0 & a_{33} & 0 \\ 0 & 0 & 0 & a_{44} \end{bmatrix}\right) \\ &\begin{bmatrix} i_{L\alpha}-i_{L\alpha ref} \\ i_{L\beta}-i_{L\beta ref} \\ v_\alpha \\ v_\beta \end{bmatrix}. \end{aligned} \tag{B.1}$$

Then, the control vectors can be calculated as

$$\begin{bmatrix} u_\alpha \\ u_\beta \end{bmatrix} = \begin{bmatrix} 1 & 0 & 0 & 0 \\ 0 & 1 & 0 & 0 \end{bmatrix} \left(\begin{bmatrix} -a_{11} & 0 & 0 & 0 \\ 0 & -a_{22} & 0 & 0 \\ 0 & 0 & -a_{33} & b_{34} \\ 0 & 0 & b_{43} & -a_{44} \end{bmatrix} * \begin{bmatrix} i_{L\alpha} - i_{L\alpha ref} \\ i_{L\beta} - i_{L\beta ref} \\ v_\alpha \\ v_\beta \end{bmatrix} - \begin{bmatrix} -R_f & 0 & -1 & 0 \\ 0 & -R_f & 0 & -1 \\ 1 & 0 & 0 & 0 \\ 0 & 1 & 0 & 0 \end{bmatrix} \begin{bmatrix} i_{L\alpha} \\ i_{L\beta} \\ v_\alpha \\ v_\beta \end{bmatrix} + \begin{bmatrix} 0 & 0 \\ 0 & 0 \\ 1 & 0 \\ 0 & 1 \end{bmatrix} \begin{bmatrix} i_{g\alpha} \\ i_{g\beta} \end{bmatrix} \right). \tag{B.2}$$

Rearranging (B.2), it can then be obtained that

$$\begin{bmatrix} u_\alpha \\ u_\beta \end{bmatrix} = \begin{bmatrix} 1\,0\,0\,0 \\ 0\,1\,0\,0 \end{bmatrix} * \left(\begin{bmatrix} -a_{11} i_{L\alpha} + a_{11}\, i_{L\alpha ref} + R_f i_{L\alpha} + v_\alpha \\ -a_{22} i_{L\beta} + a_{22} i_{L\beta ref} + R_f i_{L\beta} + v_\beta \\ -a_{33} v_\alpha + b_{34} v_\beta - i_{L\alpha} + i_{g\alpha} \\ b_{43} v_\alpha - a_{44} v_\beta - i_{L\beta} + i_{g\beta} \end{bmatrix} \right) = \begin{bmatrix} -L_f \xi_4 (i_{L\alpha ref} - i_{L\alpha}) + R_f i_{L\alpha} + v_\alpha \\ -L_f \xi_4 (i_{L\beta ref} - i_{L\beta}) + R_f i_{L\beta} + v_\beta \end{bmatrix}. \tag{B.3}$$

REFERENCES

[1] X. Gao, D. Zhou, A. Anvari-Moghaddam, and F. Blaabjerg, "Grid-following and grid-forming control in power electronic based power systems: A comparative study," in *Proc. 47th Annu. Conf. IEEE Ind. Electron. Soc.*, 2021, pp. 1–6.

[2] R. Rosso, X. Wang, M. Liserre, X. Lu, and S. Engelken, "Grid-forming converters: Control approaches, grid-synchronization, and future Trends-A review," *IEEE Open J. Ind. Appl.*, vol. 2, pp. 93–109, Apr. 2021.

[3] Q. Zhong and G. Weiss, "Synchronverters: Inverters that mimic synchronous generators," *IEEE Trans. Ind. Electron.*, vol. 58, no. 4, pp. 1259–1267, Apr. 2011.

[4] M. Colombino, D. Groß, J. Brouillon, and F. Dörfler, "Global phase and magnitude synchronization of coupled oscillators with application to the control of grid-forming power inverters," *IEEE Trans. Autom. Control*, vol. 64, no. 11, pp. 4496–4511, Nov. 2019.

[5] J. W. Simpson-Porco, F. Dörfler, and F. Bullo, "Droop-controlled inverters are Kuramoto oscillators," *IFAC Proc. Volumes*, vol. 45, no. 26, pp. 264–269, 2012.

[6] G. Filatrella, A. H. Nielsen, and N. F. Pedersen, "Analysis of a power grid using a Kuramoto-like model," *Eur. Phys. J. B*, vol. 61, no. 4, pp. 485–491, 2008.

[7] F. Dorfler and F. Bullo, "Synchronization and transient stability in power networks and nonuniform Kuramoto oscillators," *SIAM J. Control Optim.*, vol. 50, no. 3, pp. 1616–1642, 2012.

[8] H. Yu, M. A. Awal, H. Tu, I. Husain, and S. Lukic, "Comparative transient stability assessment of droop and dispatchable virtual oscillator controlled grid-connected inverters," *IEEE Trans. Power Electron.*, vol. 36, no. 2, pp. 2119–2130, Feb. 2021.

[9] M. Lu, V. Purba, S. Dhople, and B. Johnson, "Comparison of droop control and virtual oscillator control realized by Andronov-Hopf dynamics," in *Proc. IECON 46th Annu. Conf. IEEE Ind. Electron. Soc.*, 2020, pp. 4051–4056.

[10] B. B. Johnson, S. V. Dhople, A. O. Hamadeh, and P. T. Krein, "Synchronization of nonlinear oscillators in an LTI electrical power network," *IEEE Trans. Circuits Syst. I, Regular Papers*, vol. 61, no. 3, pp. 834–844, Mar. 2014.

[11] B. B. Johnson, M. Sinha, N. G. Ainsworth, F. Dörfler, and S. V. Dhople, "Synthesizing virtual oscillators to control islanded inverters," *IEEE Trans. Power Electron.*, vol. 31, no. 8, pp. 6002–6015, Aug. 2016.

[12] Y. Xue et al., "On a future for smart inverters with integrated system functions," in *Proc. IEEE Int. Symp. Power Electron. Distrib. Gener. Syst.*, 2018, pp. 1–8.

[13] P. Kundur, J. Paserba, and S. Vitet, "Overview on definition and classification of power system stability," in *Proc. CIGRE/IEEE PES Int. Symp. Qual. Secur. Electric Power Del. Syst.*, 2003, pp. 1–4.

[14] N. Hatziargyriou et al., "Definition and classification of power system stability revisited & extended," *IEEE Trans. Power Syst.*, vol. 36, no. 4, pp. 3271–3281, Jul. 2021.

[15] X. Wang, M. G. Taul, H. Wu, Y. Liao, F. Blaabjerg, and L. Harnefors, "Grid-synchronization stability of converter-based resources—An overview," *IEEE Open J. Ind. Appl.*, vol. 1, pp. 115–134, 2020.

[16] L. Zhang, L. Harnefors, and H. Nee, "Power-synchronization control of grid-connected voltage-source converters," *IEEE Trans. Power Syst.*, vol. 25, no. 2, pp. 809–820, May 2010.

[17] Y. Liao, X. Wang, F. Liu, K. Xin, and Y. Liu, "Sub-synchronous control interaction in grid-forming VSCs with droop control," in *Proc. IEEE Workshop Electron. Grid*, 2019, pp. 1–6.

[18] D. Groß, M. Colombino, J. S. Brouillon, and F. Dörfler, "The effect of transmission-line dynamics on grid-forming dispatchable virtual oscillator control," *IEEE Trans. Control Netw. Syst.*, vol. 6, no. 3, pp. 1148–1160, Sep. 2019.

[19] M. Lu, S. Dutta, V. Purba, S. Dhople, and B. Johnson, "A grid-compatible virtual oscillator controller: Analysis and design," in *Proc. IEEE Energy Convers. Congr. Expo.*, 2019, pp. 2643–2649.

[20] G. Seo, M. Colombino, I. Subotic, B. Johnson, D. Groß, and F. Dörfler, "Dispatchable virtual oscillator control for decentralized inverter-dominated power systems: Analysis and experiments," in *Proc. IEEE Appl. Power Electron. Conf. Expo.*, 2019, pp. 561–566.

[21] Q. C. Zhong and M. Stefanello, "A port-Hamiltonian control framework to render a power electronic system passive," *IEEE Trans. Autom. Control*, vol. 67, no. 4, pp. 1960–1965, Apr. 2022.

[22] L. A. B. Tôrres, J. P. Hespanha, and J. Moehlis, "Power supply synchronization without communication," in *Proc. IEEE Power Energy Soc. Gen. Meeting*, 2012, pp. 1–6.

[23] Q.-C. Zhong, *Power Electronics-Enabled Autonomous Power Systems: Next Generation Smart Grids*. Hoboken, NJ, USA: Wiley, 2020.

[24] E. M. Navarro-López and E. Licéaga-Castro, "Combining passivity and classical frequency-domain methods: An insight into decentralised control," *Appl. Math. Comput.*, vol. 215, no. 12, pp. 4426–4438, 2010.

[25] H. K. Khalil, *Nonlinear Systems*, 3rd ed. Upper Saddle River, NJ, USA: Prentice-Hall, 2002.

[26] S. Arjan van der and J. Dimitri, *Port-Hamiltonian Systems Theory: An Introductory Overview*. Hanover, MA, USA: Now Foundations and Trends, 2014, pp. 75–82.

[27] S. A. J. v. der and J. M. Schumacher, *Introduction to Hybrid Dynamical Systems*. New York, NY, USA: Springer-Verlag, 1999.

[28] Y. Liao, X. Wang, and F. Blaabjerg, "Passivity-based analysis and design of linear voltage controllers for Voltage- Source Converters," *IEEE Open J. Ind. Electron. Soc.*, vol. 1, pp. 114–126, Jun. 2020.

[29] C. Xie, K. Li, J. Zou, D. Liu, and J. M. Guerrero, "Passivity-based design of grid-side current-controlled LCL-type grid-connected inverters," *IEEE Trans. Power Electron.*, vol. 35, no. 9, pp. 9813–9823, Sep. 2020.

[30] A. Akhavan, H. R. Mohammadi, J. C. Vasquez, and J. M. Guerrero, "Passivity-based design of Plug-and-Play current-controlled grid-connected inverters," *IEEE Trans. Power Electron.*, vol. 35, no. 2, pp. 2135–2150, Feb. 2020.

[31] H. Yu, M. A. Awal, H. Tu, Y. Du, S. Lukic, and I. Husain, "Passivity-oriented discrete-time voltage controller design for grid-forming inverters," in *Proc. IEEE Energy Convers. Congr. Expo.*, 2019, pp. 469–475.

[32] H. Liu, L. Li, Y. Liu, D. Xu, and Q. Gao, "Passivity based damping design for grid-connected converter with improved stability," *IEEE Access*, vol. 7, pp. 185168–185178, 2019.

[33] Y. Qi, H. Deng, J. Wang, and Y. Tang, "Passivity-based synchronization stability analysis for power-electronic-interfaced distributed generations," *IEEE Trans. Sustain. Energy*, vol. 12, no. 2, pp. 1141–1150, Apr. 2021.

[34] A. Michel, R. Miller, and T. Wang, "Lyapunov stability of interconnected systems: Decomposition into strongly connected subsystems," *IEEE Trans. Circuits Syst.*, vol. 25, no. 9, pp. 799–809, Sep. 1978.

[35] C. Zhou and K. H. Low, "Design and locomotion control of a biomimetic underwater vehicle with fin propulsion," *IEEE/ASME Trans. Mechatronics*, vol. 17, no. 1, pp. 25–35, Feb. 2012.

[36] E. Panteley, A. Loría, and A. El-Ati, "Practical dynamic consensus of Stuart–Landau oscillators over heterogeneous networks," *Int. J. Control*, vol. 93, no. 2, pp. 261–273, 2020.

[37] Q. Qiu et al., "Origin of amplitude synchronization in coupled nonidentical oscillators," *Phys. Rev.*, vol. 101, no. 2, 2020, Art. no. 022210.
[38] L. V. Gambuzza, J. Gómez-Gardeñes, and M. Frasca, "Amplitude dynamics favors synchronization in complex networks," *Sci. Rep.*, vol. 6, no. 1, 2016, Art. no. 24915.
[39] M. C. Cross, J. L. Rogers, R. Lifshitz, and A. Zumdieck, "Synchronization by reactive coupling and nonlinear frequency pulling," *Phys. Rev. E*, vol. 73, no. 3, Mar. 2006, Art. no. 036205.
[40] M. A. Awal and I. Husain, "Unified virtual oscillator control for grid-forming and grid-following converters," *IEEE J. Emerg. Sel. Topics Power Electron.*, vol. 9, no. 4, pp. 4573–4586, Aug. 2021.
[41] R. Ortega, A. van der Schaft, B. Maschke, and G. Escobar, "Interconnection and damping assignment passivity-based control of port-controlled hamiltonian systems," *Automatica*, vol. 38, no. 4, pp. 585–596, Apr. 2002.
[42] B. Yi, R. Ortega, D. Wu, and W. Zhang, "Orbital stabilization of nonlinear systems via Mexican sombrero energy shaping and Pumping-and-Damping injection," *Automatica*, vol. 112, 2020, Art. no. 108661.
[43] D. Pan, X. Wang, F. Liu, and R. Shi, "Transient stability of voltage-source converters with grid-forming control: A design-oriented study," *IEEE J. Emerg. Sel. Topics Power Electron.*, vol. 8, no. 2, pp. 1019–1033, Jun. 2020.
[44] X. Fu et al., "Large-Signal stability of grid-forming and grid-following controls in voltage source converter: A comparative study," *IEEE Trans. Power Electron.*, vol. 36, no. 7, pp. 7832–7840, Jul. 2021.
[45] L. M. Tolbert et al., "Reconfigurable real-time power grid emulator for systems with high penetration of renewables," *IEEE Open Access J. Power Energy*, vol. 7, pp. 489–500, Oct. 2020.

Le Kong (Student Member, IEEE) received the B.S. degree in electrical engineering and automation from Nanjing University of Aeronautics and Astronautics, Nanjing, China, in 2014, and the M.S. degree in electrical engineering from National Taiwan University, Taipei, Taiwan, in 2016. She is currently working toward the Ph.D. degree in electrical engineering with the Department of Electrical Engineering and Computer Science, University of Tennessee, Knoxville, TN, USA.

From 2016 to 2017, she was an Application Engineer with the High-Power IC Department, Silergy Corporation, Hangzhou, China, focused on system analysis and design of dc converters for power units. Her current research interests include modeling, analysis, and control of dc–dc converters, power integrated circuits, and power electronics-based power grids.

Yaosuo Xue (Senior Member, IEEE) received the B.Sc. degree from East China Jiaotong University, Nanchang, China, in 1991 and the M.Sc. degree from the University of New Brunswick, Fredericton, Canada, in 2004, all in electrical engineering.

From 1991 to 2000, he was an electrical engineer-in-charge with the Ministry of Railways' 3rd Survey and Design Institute and led the traction power systems R&D for the first high-speed electric railway in China. In 2005 and 2006, he was with the Capstone Turbine Corporation as a Lead Power Electronics and Systems Engineer. He was with Siemens Corporate Research from 2009 to 2015 and led Corporate Technology North America power electronics and energy management program. He is currently a Senior R&D Staff in Oak Ridge National Laboratory. His research interests include modeling, analysis, and control of all power electronic grids.

Xue is an Associate Editor for the IEEE TRANSACTION ON POWER ELECTRONICS and IEEE OPEN ACCESS JOURNAL OF POWER AND ENERGY.

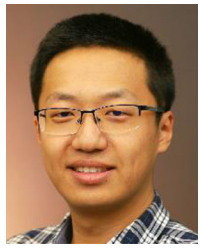

Liang Qiao (Student Member, IEEE) received the B.S. and M.S. degrees in electrical engineering from Xi'an Jiaotong University, Xi'an, China, in 2015 and 2018, respectively. He is currently working toward the Ph.D. degree in electrical engineering with the Department of Electrical Engineering and Computer Science, University of Tennessee, Knoxville, TN, USA.

His research interests include wide-bandgap devices, advanced gate drivers, and stability analysis and black-box modeling of power electronic-based power systems.

Fei (Fred) Wang (Fellow, IEEE) received the B.S. degree from Xi'an Jiaotong University, Xi'an, China, and the M.S. and Ph.D. degrees from the University of Southern California, Los Angeles, in 1982, 1985, and 1990, respectively, all in electrical engineering.

He was a Research Scientist with the Electric Power Lab, University of Southern California, from 1990 to 1992. He was with the GE Power Systems Engineering Department, Schenectady, NY, as an Application Engineer in 1992. From 1994 to 2000, he was a Senior Product Development Engineer with GE Industrial Systems, Salem, VA, USA. During 2000 to 2001, he was the Manager of Electronic and Photonic Systems Technology Lab, GE Global Research Center, Schenectady, NY, and Shanghai, China. In 2001, he was with the Center for Power Electronics Systems (CPES), Virginia Tech, Blacksburg, VA, USA, as a Research Associate Professor and became an Associate Professor in 2004. From 2003 to 2009, he was the CPES Technical Director. Since 2009, he has been with The University of Tennessee and Oak Ridge National Lab, Knoxville, TN, USA, as a Professor and the Condra Chair of Excellence in Power Electronics. His research interests include power electronics and power systems.

Dr. Wang is a fellow of the U.S. National Academy of Inventors. He is a founding member and the Technical Director of the multiuniversity NSF/DOE Engineering Research Center for Ultra-wide-area Resilient Electric Energy Transmission Networks led by The University of Tennessee.